

Attribute Prototype Network for Any-Shot Learning

Wenjia Xu^{1,7,8} · Yongqin Xian³ · Jiuniu Wang^{6,7,8} · Bernt Schiele² · Zeynep Akata^{2,4,5}

Received: date / Accepted: date

Abstract Any-shot image classification allows to recognize novel classes with only a few or even zero samples. For the task of zero-shot learning, visual attributes have been shown to play an important role, while in the few-shot regime, the effect of attributes is under-explored. To better transfer attribute-based knowledge from seen to unseen classes, we argue that an image representation with integrated attribute localization

ability would be beneficial for any-shot, i.e. zero-shot and few-shot, image classification tasks. To this end, we propose a novel representation learning framework that jointly learns discriminative global and local features using only class-level attributes. While a visual-semantic embedding layer learns global features, local features are learned through an attribute prototype network that simultaneously regresses and decorrelates attributes from intermediate features. Furthermore, we introduce a zoom-in module that localizes and crops the informative regions to encourage the network to learn informative features explicitly. We show that our locality augmented image representations achieve a new state-of-the-art on challenging benchmarks, i.e. CUB, AWA2, and SUN. As an additional benefit, our model points to the visual evidence of the attributes in an image, confirming the improved attribute localization ability of our image representation. The attribute localization is evaluated quantitatively with ground truth part annotations, qualitatively with visualizations, and through well-designed user studies.

Keywords Zero-shot learning · Few-shot learning · Attribute prototype · Attribute localization

Wenjia Xu
E-mail: xuwenjia16@mails.ucas.ac.cn

Yongqin Xian
E-mail: yongqin.xian@vision.ee.ethz.ch
The majority of the work was done when Yongqin Xian was with Max Planck Institute for Informatics

Jiuniu Wang
E-mail: wangjiuniu16@mails.ucas.ac.cn

Bernt Schiele
E-mail: schiele@mpi-inf.mpg.de

Zeynep Akata
E-mail: zeynep.akata@uni-tuebingen.de

¹ State Key Laboratory of Networking and Switching Technology, Beijing University of Posts and Telecommunications, Beijing, China

² Max Planck Institute for Informatics, Saarland Informatics Campus, Saarbrücken, Germany

³ Computer Vision Laboratory, ETH Zurich, Switzerland

⁴ University of Tübingen, Tübingen, Germany

⁵ Max Planck Institute for Intelligent Systems, Tübingen, Germany

⁶ City University of Hong Kong, Hong Kong

⁷ Aerospace Information Research Institute, Chinese Academy of Sciences

⁸ School of Electronic, Electrical and Communication Engineering, University of Chinese Academy of Sciences, China

1 Introduction

Visual attributes describe discriminative visual properties of objects shared among different classes. Attributes have been shown to be important for zero- and few-shot learning, i.e. any-shot learning, as they allow semantic knowledge transfer from known classes with abundant training samples to novel classes with only a handful of images. Most zero-shot learning (ZSL) methods (Romera-Paredes et al., 2015; Changpinyo et al., 2016; Akata et al., 2015a; Zhang et al., 2017)

rely on image representations extracted from a deep neural network pretrained on ImageNet, and essentially learn a compatibility function between the image representations and attributes. Early solutions for few-shot learning (FSL) are dominated by metric learning (Snell et al., 2017; Vinyals et al., 2016) which aims to find a better distance function, and meta-learning (Finn et al., 2017, 2018; Munkhdalai and Yu, 2017) which learns better model initialization or optimizer. Focusing on image representations that directly allow attribute localization is relatively unexplored. We argue that any-shot learning can significantly benefit from an image representation that allows localizing visual attributes in images, especially for fine-grained (Tokmakov et al., 2019; Tang et al., 2020) scenarios where local attributes are critical to distinguish two similar categories. In this work, we refer to the ability of an image representation to localize and associate an image region with a visual attribute as locality. Our goal is to improve the locality of image representations for any-shot learning.

While modern deep neural networks (He et al., 2016) encode local information and some CNN neurons are linked to object parts (Zhou et al., 2018), the encoded local information is not necessarily best suited for any-shot learning. There have been attempts to improve the locality of image representations by learning visual attention (Li et al., 2018b; Zhu et al., 2019c; Tang et al., 2020) or attribute classifiers (Sylvain et al., 2020). Zhu et al. (2019c) propose to learn channel-wise attention for bird body parts. Similarly, Zhu et al. (2019a) apply the channel grouping model (Zheng et al., 2017) to learn part-based representations and part prototypes. However, the learned latent attentions/prototypes only localize a small number of object parts, and the semantic meaning of the attentions is inducted by post-hoc observation.

Although visual attention accurately focuses on some object parts, the discovered parts and attributes are often biased towards training classes due to the learned correlations. For instance, the attributes *yellow crown* and *yellow belly* co-occur frequently (e.g. in Yellow Warbler). The model may learn such correlations as a shortcut to maximize the likelihood of training data and therefore fail to deal with unseen attributes configurations in novel classes, such as *black crown* and *yellow belly* (e.g. in Scott Oriole), as this attribute combination has not been observed before.

To improve locality and mitigate the above weaknesses of image representations, we develop a weakly supervised representation learning framework that localizes and decorrelates visual attributes. More specifically, we learn local features by injecting losses on intermediate layers of CNNs and enforcing these features to encode

visual attributes defining visual characteristics of objects. To achieve this, we learn prototypes in the feature space which define the property for each attribute, at the same time, the local image features are encouraged to be similar to the corresponding attribute prototype. It is worth noting that we use only class-level attributes and semantic relatedness of them as supervisory signal, in other words, no human-annotated association between the local features and visual attributes is given during training. We propose to alleviate the impact of incidentally correlated attributes by leveraging their semantic relatedness while learning these local features. As an additional benefit, our model points to the visual evidence of the attributes in an image, confirming the improved attribute localization ability of our image representation. The attribute attention map is obtained by measuring the similarity between local image features and attribute prototypes. We evaluate the attribute localization ability quantitatively with the ground truth part annotations, and qualitatively with visualizations. For datasets without attribute location annotations, we propose two user studies to assess the accuracy and semantic consistency of attribute attention maps, and compare our APN model with the baseline visualized by two model explanation methods, **Grad-CAM** and **CAM**.

This paper extends our NeurIPS 2020 conference paper (Xu et al., 2020) with the following additional contributions. (1) We propose to apply the Attribute Prototype Network for the any-shot image classification task, where we improve the locality of image representations. In addition to zero-shot learning, our APN is extended to few-shot learning and the more realistic generalized few-shot learning setting. We evaluate our model under both N-way-K-shot and all-way scenarios and demonstrate that the local representations encoding semantic visual attributes are beneficial for the any-shot regime in discriminating categories with only a few training samples. (2) In addition to performing classification with the original image, we propose to highlight the informative image features discovered by the attribute prototypes, which helps the network to focus on informative attribute regions and discard the noisy background. (3) We verify the effectiveness of our locality-enhanced image representations on top of five generative models and demonstrate consistent improvement over the state-of-the-art on three challenging benchmark datasets. (4) Through qualitative analysis among three benchmark datasets and qualitative ablation study, we demonstrate that our proposed model helps to learn accurate attribute prototypes and produce compact attribute attention maps for each image. Quantitative evaluation indicates that our model outperforms other weakly

supervised attribute localization methods by a large margin. (5) We propose two well-designed user studies to evaluate the accuracy and semantic consistency of the attribute attention maps, which is an effective evaluation protocol in the absence of ground truth annotations.

2 Related work

Zero-shot learning. The aim of zero-shot learning is to classify the object classes that are not observed during training (Lampert et al., 2009). The key insight is to transfer knowledge learned from seen classes to unseen classes with class embeddings that capture similarities between them. Many classical approaches (Romera-Paredes et al., 2015; Changpinyo et al., 2016; Akata et al., 2015a; Zhang et al., 2017; Xian et al., 2016; Wang and Chen, 2017) learn a compatibility function between image and class embedding spaces. Recent advances in zero-shot learning mainly focus on learning better visual-semantic embeddings (Liu et al., 2018; Zhang et al., 2017; Jiang et al., 2019; Cacheux et al., 2019; Wan et al., 2021; Li et al., 2020) or training generative models to synthesize features (Xian et al., 2018, 2019b; Zhu et al., 2019b, 2018; Kumar Verma et al., 2018; Schonfeld et al., 2019a; Changpinyo et al., 2020). Those approaches are limited by their image representations, which are often extracted from ImageNet-pretrained CNNs or finetuned CNNs on the target dataset with a cross-entropy loss.

Despite its importance, image representation learning is relatively under-explored in ZSL. Recently, Yu et al. (2018) propose to weigh different local image regions by learning attentions from class embeddings. Zhu et al. (2019c) extend the attention idea to learn multiple channel-wise part attentions. Sylvain et al. (2020) show the importance of locality and compositionality of image representations for ZSL. In our work, instead of learning visual attention like Zhu et al. (2019c) and Yu et al. (2018), we propose to improve the locality of image features by learning a prototype network that is able to localize different attributes in an image.

Few-shot learning. Given a large number of training samples from the base classes, few-shot learning (FSL) aims to recognize novel classes with a handful of (typically 1–10) labeled examples. The data efficiency problem challenges the traditional classification task, and much effort has been devoted to overcome the data sparsity issue. Metric learning based methods tackle this problem by comparing the distance between images, i.e. Euclidean distance to class prototypes (Snell et al., 2017), cosine similarity (Vinyals et al., 2016), etc. Meta learning based methods aim to learn a good model

initialization (Finn et al., 2017, 2018; Rusu et al., 2019) or optimizer (Ravi and Larochelle, 2017; Munkhdalai and Yu, 2017), so that the classifiers for novel classes can be learned with a few labeled examples and a small number of gradient update steps. However, meta-learning may not sufficiently handle the domain shift between base and novel classes (Chen et al., 2019b), and has difficulty when scaling to a large number of training samples (Xian et al., 2019b). This motivates data augmentation via feature synthesis which directly tackles the data deficiency problem by generating novel training examples (Guan et al., 2020; Xian et al., 2019b), e.g. Hariharan and Girshick (2017) and Qi et al. (2018) propose to hallucinate additional training examples for novel classes.

Existing FSL methods usually rely on prior knowledge from only visual modality, while in zero-shot learning, multi-modality data such as word embeddings (Xian et al., 2019a) and attributes (Lampert et al., 2009) have been adopted and achieve promising results. There are some attempts in applying multi-modality to aid representation learning in FSL (Sylvain et al., 2020; Tokmakov et al., 2019; Tang et al., 2020) or to train a feature generator with GANs (Xian et al., 2019b; Guan et al., 2020). A few works have focused on enhancing the compositionality (Tokmakov et al., 2019) with the help of attributes or learning pose-normalized image representations (Tang et al., 2020), making the representation invariant to the spatial deformations and environmental changes. In this paper, we focus on learning locality-augmented image representations with the help of class attributes to aid the classification task under a low-data regime. We demonstrate that local information encoded in the image representation helps generative models to synthesize discriminative features.

Prototype learning. Prototype networks (Yang et al., 2018; Wang et al., 2019) learn a metric space where the labeling is done by calculating the distance between the test image and prototypes of each class. Prototype learning is considered to be more robust when handling open-set recognition (Yang et al., 2018; Shu et al., 2020) and few-shot learning (Snell et al., 2017; Gao et al., 2019; Oreshkin et al., 2018). Some methods (Arik and Pfister, 2019; Yeh et al., 2018; Li et al., 2018a) base the network classification decision on learned prototypes. Instead of building sample-based prototypes, Chen et al. (2019a) dissect the image and find several prototypical parts for each object category, then classify images by combining evidences from prototypes. Similarly, Zhu et al. (2019a) use the channel grouping model (Zheng et al., 2017) to learn part-based representations and part prototypes.

In contrast, we treat each channel equally and use spatial features associated with input image patches

to learn attribute prototypes. Chen et al. (2019a) and Zhu et al. (2019c,a) learn latent attention or prototypes during training and induct the semantic meaning of the prototypes in a post-hoc manner. Their attribute or part localization ability is limited, e.g. Zhu et al. (2019c) can only localize two parts. To address those limitations, our method learns prototypes that represent the attributes/parts where each prototype corresponds to a specific attribute. The attribute prototypes are shared among different classes and encourage knowledge transfer from seen classes to unseen classes, yielding better image representation for zero-shot learning and few-shot learning.

Locality and representation learning. Here we define the local feature as the image feature encoded from a local image region. Local features have been extensively investigated for representation learning (Hjelm et al., 2019; Wei et al., 2019; Noroozi and Favaro, 2016), and are commonly used in person re-identification (Sun et al., 2018; Wang et al., 2018a), image captioning (Anderson et al., 2018; Li et al., 2017) and fine-grained classification (Zheng et al., 2017; Fu et al., 2017; Zhang et al., 2016b). Hjelm et al. (2019) indicate that maximizing the mutual information between the representation and local regions of the image can significantly improve a representation’s suitability for downstream tasks. Thanks to its locality-aware architecture, CNNs (He et al., 2016) exploit local information intrinsically. Our work is related to methods that draw attention to local features (Kim et al., 2018; Sun et al., 2018). Zheng et al. (2017) generate the attention for discriminative bird parts by clustering spatially-correlated channels. Instead of operating on feature channels, we focus on the spatial configuration of image features and improve the locality of our representation. Besides, our work is supervised by the class attributes, and no part or bounding box annotation is required.

Our work is also related to the methods that localize the main object in a weakly supervised way and discard the irrelevant background for image classification (Zhang et al., 2021a; Wei et al., 2017). Wei et al. (2017) aggregate the activation map from the last CNN layer (before global average pooling) and select the highest activated location to filter the final representation for the target image. Zhang et al. (2021a) improve the localization accuracy by introducing multi-layer activation maps. While in our network, we aim to search for the informative image regions that contain important attributes for zero- and few-shot learning. Unlike previous pioneers utilizing intermediate activation maps to localize the informative area, we select the image regions highlighted by the attribute prototypes. Since most of the datasets lack ground truth

attribute location annotation, e.g. AWA2 and SUN, we design two user studies to assess the accuracy and semantic consistency.

3 Attribute Prototype Network

In the following, we describe our end-to-end trained attribute prototype network (APN) that improves the attribute localization ability of the image representation, i.e. locality. We first define our zero-shot learning and few-shot learning problem. We then introduce in detail the three modules in our framework, the base module (**BaseMod**), the prototype module (**ProtoMod**), and the Zoom-In Module (**ZoomInMod**) as shown in Figure 1. At the end of the section, we describe how we perform ZSL and FSL and how the locality enables attribute localization.

Problem Definition The training set consists of labeled images and attributes from seen classes, i.e. $S = \{x, y, \phi(y) | x \in \mathcal{X}, y \in \mathcal{Y}^s\}$. Here, x denotes an image in the RGB image space \mathcal{X} , y is its class label, and $\phi(y) \in \mathbb{R}^K$ is the class embedding (i.e. a class-level attribute vector annotated with K different visual attributes). Here we use \mathcal{Y}^n to denote the unseen class label set in ZSL and the novel class in FSL for convenience. The class embeddings of unseen classes, i.e. $\{\phi(y) | y \in \mathcal{Y}^n\}$, are also known. The goal for ZSL is to predict the label of images from unseen classes, i.e. $\mathcal{X} \rightarrow \mathcal{Y}^n$, while for generalized ZSL (GZSL) (Xian et al., 2019a) the goal is to predict images from both seen and unseen classes, i.e. $\mathcal{X} \rightarrow \mathcal{Y}^n \cup \mathcal{Y}^s$. Few-shot learning (FSL) and generalized few-shot learning (GFSL) are defined similarly. The main difference lies that instead of only knowing the attributes of novel classes in ZSL, FSL also gets a few training samples from each novel class.

3.1 Base Module (**BaseMod**) for global feature learning

The base module (**BaseMod**) learns discriminative visual features for classification. Given an input image x , the **Image Encoder** (a CNN backbone) converts it into a feature representation $f(x) \in \mathbb{R}^{H \times W \times C}$ where H , W and C denote the height, width, and channel respectively. **BaseMod** then applies global average pooling over the H and W to learn a global discriminative feature $g(x) \in \mathbb{R}^C$:

$$g(x) = \frac{1}{H \times W} \sum_{i=1}^H \sum_{j=1}^W f_{i,j}(x), \quad (1)$$

where $f_{i,j}(x) \in \mathbb{R}^C$ is extracted from the feature $f(x)$ at spatial location (i, j) (blue box in Figure 1).

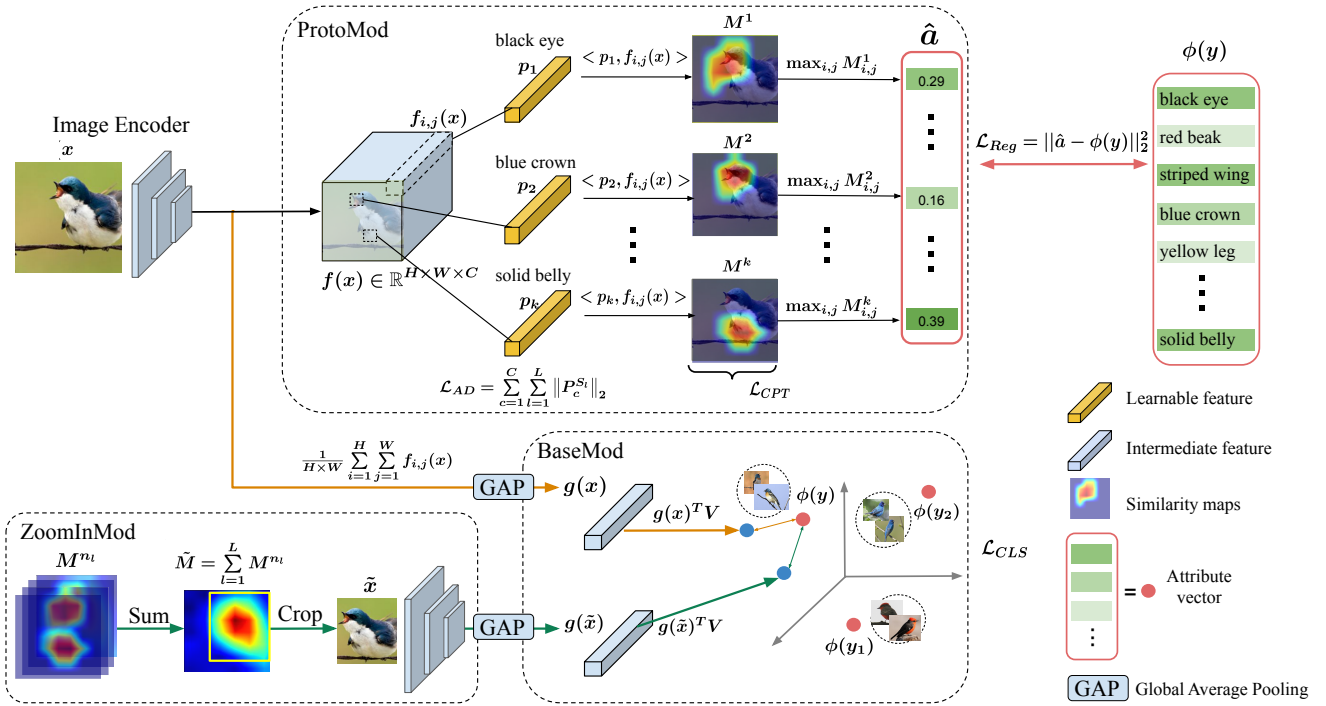


Fig. 1: Our attribute prototype network (APN) consists of an **Image Encoder** extracting image features $f(x)$, a **BaseMod** performing classification, a **ProtoMod** learning attribute prototypes p_k and localizing them with similarity maps M^k , and a **ZoomInMod** cropping the informative image region \tilde{x} covered by attribute similarity maps. The end-to-end training of APN encourages the image feature to contain both global information which is discriminative for classification and local information which is crucial to localize and predict attributes.

Visual-semantic embedding layer. In contrast to standard CNNs with fully connected layers to compute class logits, we further improve the expressiveness of the image representation using attributes. In detail, a linear layer with parameter $V \in \mathbb{R}^{C \times K}$ maps the visual feature $g(x)$ into the class embedding (e.g. attribute) space. The dot product between the projected visual feature and every class embedding is computed to produce class logits $s = g(x)^T V \phi(y)$, followed by the cross-entropy loss encouraging the image to have a high compatibility score with its corresponding attribute vector. Given a training image x with a label y and an attribute vector $\phi(y)$, the classification loss \mathcal{L}_{CLS} is:

$$\mathcal{L}_{CLS} = -\log \frac{\exp(s)}{\sum_{y^s} \exp(s_j)}, \quad (2)$$

where $s_j = g(x)^T V \phi(y_j)$, $y_j \in \mathcal{Y}^s$. The visual-semantic embedding layer and the CNN backbone are optimized jointly to finetune the image representation guided by the attribute vectors.

3.2 Prototype Module (ProtoMod) for local feature learning

The global features learned from **BaseMod** may be biased to seen classes because they mainly capture global context, shapes and other discriminative features that may be indicative of training classes. To improve the locality of the image representation, we propose a prototype module (**ProtoMod**) focusing on the local features that are often shared across seen and unseen classes.

Attribute prototypes. **ProtoMod** takes as input the feature $f(x) \in \mathbb{R}^{H \times W \times C}$ produced by the **Image Encoder** where the local feature $f_{i,j}(x) \in \mathbb{R}^C$ at spatial location (i, j) encodes information of local image regions. Our main idea is to improve the locality of the image representation by enforcing those local features to encode visual attributes that are critical for ZSL. Specifically, we learn a set of attribute prototypes $P = \{p_k \in \mathbb{R}^C\}_{k=1}^K$ to predict attributes from those local features, where p_k denotes the prototype for the k -th attribute. As a schematic illustration, p_1 and p_2 in Figure 1 correspond to the prototypes for *black eye* and *blue crown* respectively. For each attribute (e.g. k -th

attribute), we produce a similarity map $M^k \in \mathbb{R}^{H \times W}$ where each element is computed by a dot product between the attribute prototype p_k and each local feature, i.e. $M_{i,j}^k = \langle p_k, f_{i,j}(x) \rangle$. Afterwards, we predict the k -th attribute \hat{a}_k by taking the maximum value in the similarity map M^k :

$$\hat{a}_k = \max_{i,j} M_{i,j}^k. \quad (3)$$

Other alternative operations such as average pooling and weighted average pooling are also performed for consideration, while max-pooling works the best, since it associates each visual attribute with its closest local feature and allows the network to efficiently localize attributes.

Attribute regression loss. The class-level attribute vectors supervise the learning of attribute prototypes. We consider the attribute prediction task as a regression problem and minimize the Mean Square Error (MSE) between the ground truth attributes $\phi(y)$ and the predicted attributes \hat{a} :

$$\mathcal{L}_{Reg} = \|\hat{a} - \phi(y)\|_2^2, \quad (4)$$

where y is the ground truth class. By optimizing the regression loss, we enforce the local features to encode semantic attributes, improving the locality of the image representation.

Attribute decorrelation loss. Visual attributes are often correlated with each other as they frequently co-occur, e.g. *blue crown* and *blue back* for Blue Jay birds. Consequently, the network may use those correlations as a useful signal and fails to recognize unknown combinations of attributes in novel classes. Therefore, we propose to constrain the attribute prototypes by encouraging feature competition among unrelated attributes and feature sharing among related attributes. To represent the semantic relation of attributes, we divide all K attributes into L disjoint groups, encoded as L sets of attribute indices S_1, \dots, S_L . We directly adopt the disjoint attribute groups defined by the datasets (Wah et al., 2011; Lampert et al., 2009; Patterson et al., 2014). Two attributes are in the same group if they have some semantic tie, e.g. *blue eye* and *black eye* are in the same group as they describe the same body part, while *blue back* belongs to another group. For each attribute group S_l , its attribute prototypes $\{p_k | k \in S_l\}$ can be concatenated into a matrix $P^{S_l} \in \mathbb{R}^{C \times |S_l|}$, and $P_c^{S_l}$ is the c -th row of P^{S_l} . We adopt the attribute decorrelation (AD) loss inspired from Jayaraman et al. (2014):

$$\mathcal{L}_{AD} = \sum_{c=1}^C \sum_{l=1}^L \|P_c^{S_l}\|_2. \quad (5)$$

This regularizer enforces feature competition across attribute prototypes from different groups and feature sharing across prototypes within the same groups, which helps decorrelate unrelated attributes.

Similarity map compactness regularizer. In addition, we would like to constrain the similarity map such that it concentrates on its peak region rather than disperses on other locations. Therefore, we apply the following compactness regularizer (Zheng et al., 2017) on each similarity map M^k ,

$$\mathcal{L}_{CPT} = \frac{1}{KHW} \sum_{k=1}^K \sum_{i=1}^H \sum_{j=1}^W M_{i,j}^k \left[(i - \tilde{i})^2 + (j - \tilde{j})^2 \right], \quad (6)$$

where $(\tilde{i}, \tilde{j}) = \arg \max_{i,j} M_{i,j}^k$ denotes the coordinate for the maximum value in M^k . This objective enforces the attribute prototype to resemble only a small number of local features, resulting in a compact similarity map.

3.3 Zoom-In Module (ZoomInMod) for attribute prototype-informed feature learning

Previous works have shown that the informative attributes are critical to the knowledge transfer in zero-shot learning (Liu et al., 2019; Guo et al., 2018; Liu et al., 2014). We propose a Zoom-In Module (ZoomInMod) to highlight the image regions covered by the informative attribute similarity maps and discard the irrelevant image regions. Instead of performing classification in **BaseMod** with the original image x (the orange pipeline in Figure 1), the Zoom-In Module crops out the illuminating image region \tilde{x} that are attended by informative attributes and feed the image into **BaseMod** (the green pipeline). As illustrated in Figure 1 (left), we sum up the attribute similarity maps for the most informative attribute in each attribute group to form the attention map \tilde{M} :

$$\tilde{M} = \sum_{l=1}^L M^{n_l}, \text{ where } n_l = \arg \max_{k \in S_l} a_k. \quad (7)$$

M^{n_l} indicates the attribute similarity map, and n_l is the index of the highest predicted (most informative) attribute in the l -th attribute group (e.g. the attention maps for “white belly” in “belly” attribute group). We follow Zhang et al. (2021a) to binarize the informative attention map \tilde{M} with the average attention value to form a mask A :

$$A_{i,j} = \begin{cases} 1 & \text{if } \tilde{M}_{i,j} \geq \bar{m} \\ 0 & \text{if } \tilde{M}_{i,j} < \bar{m} \end{cases}, \text{ where } \bar{m} = \frac{1}{HW} \sum_{i=1}^H \sum_{j=1}^W \tilde{M}_{i,j}.$$

(8)

(12)

We upsample the binary mask A to the size of the input image, and use the smallest bounding box covering the non-zero area to crop the original image. Then we feed the cropped image \tilde{x} into the **Image Encoder**. Note that there are no parameters in the **ZoomInMod**. When **ZoomInMod** is working, the **BaseMod** takes into two inputs, i.e. the original image x and the Zoom-In image \tilde{x} , and maps the visual feature $g(x)$ and $g(\tilde{x})$ into the class embedding space with visual-semantic embedding layer V . We sum up the class logits for each image to induct the predicted class. So the overall compatibility scores are as follows:

$$s = g(x)^T V \phi(y) + g(\tilde{x})^T V \phi(y), \quad (9)$$

used to optimize the classification loss in Equation (2).

Joint global and local feature learning. Our full model optimizes the CNN backbone, **BaseMod** and **ProtoMod** simultaneously with the following objective function,

$$\mathcal{L}_{APN} = \mathcal{L}_{CLS} + \lambda_1 \mathcal{L}_{Reg} + \lambda_2 \mathcal{L}_{AD} + \lambda_3 \mathcal{L}_{CPT}, \quad (10)$$

where λ_1, λ_2 , and λ_3 are hyper-parameters. The joint training improves the locality of the image representation that is critical for any-shot generalization as well as the discriminability of the features. In the following, we will explain how we perform any-shot inference and attribute localization.

3.4 Zero- and few-shot learning

Once our full model is trained, the visual-semantic embedding layer of the **BaseMod** can be directly used for zero-shot learning inference, which is similar to ALE (Akata et al., 2015a). For ZSL, given an image x , we generate the ZoomIn image \tilde{x} through the **ProtoMod** and **ZoomInMod**, and feed them into the **BaseMod**. The classifier searches for the class embedding with the highest compatibility via

$$\hat{y} = \arg \max_{\tilde{y} \in \mathcal{Y}^n} (g(x)^T V \phi(\tilde{y}) + g(\tilde{x})^T V \phi(\tilde{y})). \quad (11)$$

For generalized zero-shot learning (GZSL), we need to predict both seen and unseen classes. The extreme data imbalance issue will result in predictions to be biased towards seen classes (Chao et al., 2016). To fix this issue, we apply Calibrated Stacking (CS) (Chao et al., 2016) to reduce the seen class scores by a constant factor. Specifically, the GZSL classifier is defined as,

$$\hat{y} = \arg \max_{\tilde{y} \in \mathcal{Y}^n \cup \mathcal{Y}^s} (g(x)^T V \phi(\tilde{y}) + g(\tilde{x})^T V \phi(\tilde{y})) - \gamma \mathbb{I}[\tilde{y} \in \mathcal{Y}^s],$$

where the indicator $\mathbb{I}[\cdot] = 1$ if \tilde{y} is a seen class and 0 otherwise, γ is the calibration factor tuned on a held-out validation set.

Our model aims to improve the image representation for novel class generalization and is applicable to other ZSL methods (Zhu et al., 2019b; Xian et al., 2018; Changpinyo et al., 2016), i.e. once learned, our features can be applied to any ZSL model (Zhu et al., 2019b; Xian et al., 2018; Changpinyo et al., 2016). Therefore, in addition to the above classifiers, we use image features $g(x)$ extracted from the **Image Encoder**, and train several state-of-the-art ZSL approaches on top of our features, e.g. ABP (Zhu et al., 2019b), f-VAEGAN-D2 (Xian et al., 2019b), and TF-VAEGAN (Narayan et al., 2020).

Our APN network can be adapted to the task of few-shot learning (FSL) by replacing the feature extraction network in FSL methods with our APN network. During the representation learning stage, we train the feature extractor $f(\cdot)$ using the training examples in the base classes $S = \{x, y, \phi(y) | x \in \mathcal{X}, y \in \mathcal{Y}^s\}$, and train the network with the original FSL training loss as well as our \mathcal{L}_{APN} loss. With the help of the attribute prototype network, we can learn locality augmented representations that are discriminative for FSL models (Yang et al., 2020) and boost their performance. Besides, the locality augmented image representations in our model are applicable to the data synthesis based few-shot learning methods (Xian et al., 2019b; Guan et al., 2020). We use image features $g(x)$ extracted from the **Image Encoder** to train several state-of-the-art generative FSL approaches (Narayan et al., 2020; Xian et al., 2019b) and improve their performance.

3.5 Attribute localization

As a benefit of the improved local features, our approach is capable of localizing different attributes in the image by inspecting the similarity maps produced by the attribute prototypes. More specifically, we upsample the similarity map M^k to the size of the input image with bilinear interpolation. The area with the maximum responses then encodes the image region that gets associated with the k -th attribute. Figure 1 illustrates the attribute regions of *black eye*, *blue crown* and *solid belly* from the learned similarity maps. It is worth noting that our model only relies on class-level attributes and semantic relatedness of them, i.e. attribute groups, as the auxiliary information and does not need any annotation of part locations.

	ZSL			Part localization on CUB						
Method	CUB	AWA2	SUN	breast	belly	back	head	wing	leg	Mean
BaseMod	70.0	64.9	60.0	40.3	40.0	27.2	24.2	36.0	16.5	30.7
+ \mathcal{L}_{Reg}	71.5	66.3	60.9	41.6	43.6	25.2	38.8	31.6	30.2	35.2
+ \mathcal{L}_{AD}	71.8	67.7	61.4	60.4	52.7	25.9	60.2	52.1	42.4	49.0
+ \mathcal{L}_{CPT}	72.0	68.4	61.6	63.1	54.6	30.5	64.1	55.9	50.5	52.8
+ ZoomInMod	75.0	69.9	61.5	67.8	55.9	29.4	68.7	49.2	49.1	53.4

Table 1: Ablation study of ZSL on CUB, AWA2, SUN (left, top-1 accuracy) and part localization on CUB (right, PCP). We train a single **BaseMod** with the original input x as the baseline. Note that the last row represents our full model **APN**, which combines **BaseMod** and **ProtoMod** (trained with \mathcal{L}_{CLS} , \mathcal{L}_{Reg} , \mathcal{L}_{AD} , \mathcal{L}_{CPT}), and the **ZoomInMod**.

4 Experiments

In the following, we first introduce the datasets. Then we evaluate our attribute prototype network in both zero-shot learning as well as the attribute localization performance. We finally evaluate our network on few-shot learning.

Datasets. We conduct the experiments on three widely used benchmark datasets. CUB (Wah et al., 2011) is a fine-grained dataset containing 11,788 images from 200 bird classes with 312 attributes. Following SPDA-CNN (Zhang et al., 2016a), we define 7 body parts for all the birds in CUB dataset, i.e. *belly*, *breast*, *back*, *wing*, *head*, *leg*, *tail*. Part related attributes are divided into seven part groups. SUN (Patterson et al., 2014) is a fine-grained dataset consisting of 14,340 images from 717 scene classes, with 102 attributes divided into 4 groups, describing the *functions*, *materials*, *surface properties* and *spatial envelope* of scene images. AWA2 (Xian et al., 2019a) is a coarse-grained dataset containing 37,322 images of 50 animal classes with 85 attributes. We follow Lampert et al. (2009) to divide 85 attributes into 9 groups, describing various properties of animals, i.e. *color*, *texture*, *shape*, *body parts*, *behaviour*, *nutrition*, *activity*, *habitat* and *character*. For zero-shot learning, we split the seen/unseen classes following Xian et al. (2019a) to avoid overlap between novel images and ImageNet 1K images.

For few-shot learning, we follow two kinds of evaluation protocols. In the N-way-K-shot scenario, the task is to train a classifier with K samples from N classes, to correctly classify the query samples. Following Yang et al. (2020), we randomly split the CUB dataset into 100 base, 50 validation, and 50 novel classes. In addition to the widely used N-way-K-Shot benchmarks, we also focus on a more realistic setting, i.e. the all-way benchmark (Tang et al., 2020; Wang et al., 2018b; Hariharan and Girshick, 2017). The classifiers are supposed to recognize all the categories simultaneously, i.e. $\mathcal{X} \rightarrow \mathcal{Y}^n$ for FSL and $\mathcal{X} \rightarrow \mathcal{Y}^n \cup \mathcal{Y}^s$ for generalized

FSL. In the all-way scenario, we follow Xian et al. (2019b) to split three benchmark datasets, i.e. CUB, AWA2, and SUN.

Implementation. To train the attribute prototype network, we adopt ResNet101 (He et al., 2016) pre-trained on ImageNet (Deng et al., 2009) as the backbone, and jointly finetune the entire model in an end-to-end fashion to improve the image representation. We use the Adam optimizer (Kingma and Ba, 2015) with $\beta_1 = 0.5$ and $\beta_2 = 0.999$. The learning rate is initialized as 10^{-6} and decreased every ten epochs by a factor of 0.9. Hyperparameters in our model are obtained by grid search on the validation set (Xian et al., 2019a). We set λ_1 as ranges from 0.01 to 0.1 for three datasets, λ_2 as 0.01, and λ_3 as 0.2. The factor γ for Calibrated Stacking is set to 0.7 for CUB, 0.85 for AWA2, and 0.4 for SUN.

Evaluation metrics We follow the same evaluation protocol as demonstrated in Xian et al. (2019a) and Xian et al. (2019b): for ZSL/FSL we report average top-1 accuracy for unseen (novel) classes; for GZSL we report average top-1 accuracy for both seen (s) and unseen (u) classes, as well as their harmonic mean (H); for GFSL we report average top-1 accuracy for both seen and novel classes.

4.1 Zero-shot learning

In this section, we present an ablation study of our framework in the ZSL setting, and then we present a comparison with the state-of-the-art in ZSL and GZSL settings.

Ablation study. To measure the influence of each model component on the extracted image representation, we design an ablation study where we train a single **BaseMod** with cross-entropy loss as the baseline, and four variants of **APN** by adding the **ProtoMod** and the three loss functions, attribute regression loss \mathcal{L}_{Reg} , attribute decorrelation loss \mathcal{L}_{AD} , and compactness regularizer \mathcal{L}_{CPT} gradually, and finally we add the

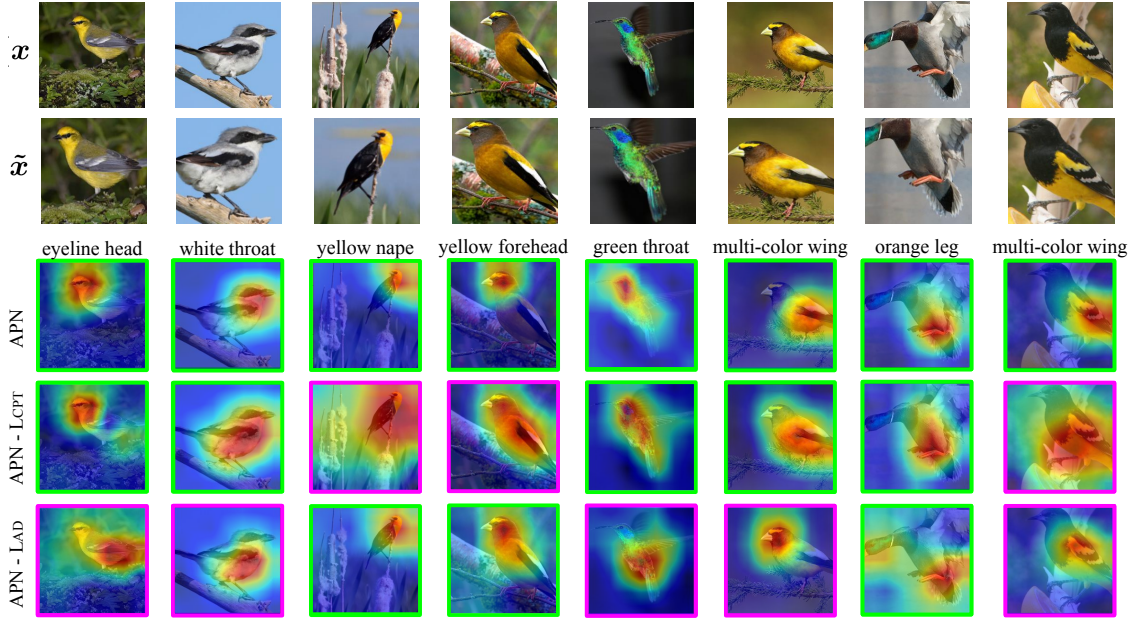


Fig. 2: The qualitative ablation study. We display the original image, the Zoom-In image from ZoomInMod in the first and second row. From the third to the fifth row, we show the attribute similarity maps from our APN model, our model trained without \mathcal{L}_{CPT} , and our model trained without \mathcal{L}_{AD} , respectively. The text above the attribute similarity maps indicates the attribute name. Green (purple) box outside the image indicates a correct (incorrect) localization by our model.

ZoomInMod to generate a ZoomIn image as the input for the BaseMod. Our results on CUB, AWA2 and SUN presented in Table 1 (left) demonstrate that the full APN model improve ZSL accuracy over BaseMod consistently, by 5.0% (CUB), 5.0%(AWA2), and 1.5% (SUN). The attribute regression loss supervises the learning of each attribute prototype and enforces the local image features to contain attribute information, which boosts the performance by 1.5% (CUB), 1.4% (AWA2), and 0.9% (SUN). This indicates that adding locality to the image representation can help the network to learn discriminative features and significantly improve the performance of unseen classes. The attribute decorrelation loss, which suppresses the unwanted attribute co-occurrence and helps to recognize unknown combinations of attributes in novel classes, provides accuracy gains on AWA2 (1.4%), CUB (0.3%), and SUN (0.5%). The compactness loss, which constrains the attribute attention maps, does not influence ZSL accuracy much. The ZoomInMod highlights the informative image region and provides significant performance gain for CUB (3.0%) and AWA2 (1.5%).

The accuracy improvement on SUN is not as great as that on CUB and AWA2 for the following reasons. First, APN aims to learn local image features by regressing and decorrelating attributes, which works well for local and visually-grounded attributes. Most

attributes in CUB and AWA2 are related to the local visual properties of the birds and animals. However, the attributes of SUN are designed to be global and abstract (Patterson et al., 2014), thus sometimes can not help with learning locality image features. Second, the data distribution of SUN is quite different from CUB and AWA2. The datasets for bird (CUB) and animal (AWA2) classification contain main object and discriminative regions. However, dataset SUN is for scene classification, where each element in a scene is crucial in discriminating it from other categories. For instance, the “glacier” in Figure 4 (right, column 2) consists of mountains, snow, and sky, and the global feature of the whole scene can lead to good predictions. Emphasizing local features as APN and the ZoomInMod can not help much.

The qualitative ablation of our APN network is shown in Figure 2. We display the Zoom-In image \tilde{x} generated by the ZoomInMod in the second row. The Zoom-In image \tilde{x} accurately crops out the objects, e.g. the birds in the corner (row 2, column 3), and discards the noisy background. We qualitatively ablate the attribute decorrelation loss \mathcal{L}_{AD} and the compactness regularizer \mathcal{L}_{CPT} by visualizing the attribute similarity maps generated by different models.

Adding the ZoomInMod increases the model complexity by around two times, e.g. increasing FLOPs from

Method	Zero-Shot Learning (ZSL)			Generalized Zero-Shot Learning (GZSL)								
	CUB	AWA2	SUN	CUB			AWA2			SUN		
	T1	T1	T1	u	s	H	u	s	H	u	s	H
SGMA (Zhu et al., 2019c)	71.0	68.8	—	36.7	71.3	48.5	37.6	87.1	52.5	—	—	—
AREN (Xie et al., 2019)	71.8	67.9	60.6	63.2	69.0	66.0	54.7	79.1	64.7	40.3	32.3	35.9
§ LFGAA+Hybrid (Liu et al., 2019)	67.6	68.1	61.5	36.2	80.9	50.0	27.0	93.4	41.9	18.5	40.4	25.3
APN [‡] (Xu et al., 2020)	72.0	68.4	61.6	65.3	69.3	67.2	56.5	78.0	65.5	41.9	34.0	37.6
APN (Ours)	75.0	69.9	61.5	67.4	71.6	69.4	61.9	79.4	69.6	40.2	35.2	37.5
LisGAN (Li et al., 2019a)	58.8	70.6	61.7	46.5	57.9	51.6	52.6	76.3	62.3	42.9	37.8	40.2
CLSWGAN (Xian et al., 2018)	57.3	68.2	60.8	43.7	57.7	49.7	57.9	61.4	59.6	42.6	36.6	39.4
FREE (Chen et al., 2021)	—	—	—	55.7	59.9	57.7	60.4	75.4	67.1	47.4	37.2	41.7
ABP* (Zhu et al., 2019b)	70.7	68.5	62.6	61.6	73.0	66.8	53.7	72.1	61.6	43.3	39.3	41.2
APN+ABP (Ours)	73.2	73.9	63.4	65.5	74.6	69.8	57.4	72.3	64.0	46.2	37.8	41.6
† CVC* (Li et al., 2019b)	70.0	64.6	61.0	61.1	74.2	67.0	57.4	83.1	67.9	36.3	42.8	39.3
APN+CVC (Ours)	71.0	71.2	60.6	62.0	74.5	67.7	63.2	81.0	71.0	37.9	45.2	41.2
GDAN* (Huang et al., 2019)	—	—	—	65.7	66.7	66.2	32.1	67.5	43.5	38.1	89.9	53.4
APN+GDAN (Ours)	—	—	—	67.9	66.7	67.3	35.5	67.5	46.5	41.4	89.9	56.7
f-VAEGAN-D2* (Xian et al., 2019b)	72.9	70.3	65.6	63.2	75.6	68.9	57.1	76.1	65.2	50.1	37.8	43.1
APN+f-VAEGAN-D2* (Ours)	73.9	73.4	65.9	65.5	75.6	70.2	62.7	68.9	65.7	49.9	39.3	43.8
TF-VAEGAN* (Narayan et al., 2020)	74.3	73.4	65.4	65.5	75.1	70.0	58.3	81.6	68.0	45.3	40.7	42.8
APN+TF-VAEGAN (Ours)	74.7	73.5	66.3	65.6	76.3	70.6	60.9	79.1	68.8	52.6	37.3	43.7

Table 2: Comparing our APN model with the state-of-the-art on CUB, AWA2 and SUN datasets. † and § indicate generative and non-generative representation learning methods respectively. AREN (Xie et al., 2019) and APN (Ours) uses Calibrated Stacking (Chao et al., 2016) for GZSL. We denote the attribute prototype network trained without ZoomInMod in Xu et al. (2020) as APN[‡], and represent our full model with ZoomInMod as APN in this paper. For fair comparison, the generative models marked with * (e.g. ABP*) use *finetuned features* extracted from ResNet101, while the models below, e.g. APN+ABP(Ours), use our *APN features*. We measure top-1 accuracy (T1) in ZSL, top-1 accuracy on seen/unseen (s/u) classes and their harmonic mean (H) in GZSL.

7.9 GMac to 15.7 GMac, increasing memory from 5,216 MiB to 9,052 MiB. However, the training process is still efficient, which will finish in 48 minutes on CUB dataset with a single NVIDIA V100 GPU.

From Figure 2 (row 3-5), we have the following observations. First, the compactness regularizer \mathcal{L}_{CPT} helps the model to generate compact attention maps that focus on the most salient attribute region. For instance, our APN model attends to the correct image region when predicting attributes, and the model works well even when localizing small attribute regions, e.g. the “yellow nape”, “yellow forehead” and “multi-colored wing” (row 3, column 3,4,6). While the APN – \mathcal{L}_{CPT} model produces disperse attention maps and results in inaccurate attribute similarity maps. When predicting attributes “yellow nape” and “yellow forehead” (row 4, column 3,4), the model spreads attention over the whole bird body. This observation agrees with the quantitative results in Table 1 where \mathcal{L}_{CPT} loss improves the part localization score.

Second, the decorrelation loss \mathcal{L}_{AD} helps the model to avoid attribute correlations and results in precise attention maps. For example, the model APN – \mathcal{L}_{AD} misunderstands “white throat” with “white belly” (row

5, column 2), and “green throat” with “green belly” (row 5, column 5). The reason might be the model APN – \mathcal{L}_{AD} learns similar prototypes for two attributes since they share often co-occurring color properties. While the model APN trained with attribute decorrelation loss forces attribute prototypes from different body parts to be different and correctly localizes the corresponding area.

Comparing with the SOTA. We compare our attribute prototype network (APN) with two groups of state-of-the-art models: non-generative models, i.e. SGMA (Zhu et al., 2019c), AREN (Xie et al., 2019), LFGAA+Hybrid (Liu et al., 2019); and generative models, i.e. LisGAN (Li et al., 2019a), CLSWGAN (Xian et al., 2018), FREE (Chen et al., 2021), ABP (Zhu et al., 2019b), CVC (Li et al., 2019b), GDAN (Huang et al., 2019), f-VAEGAN-D2 (Xian et al., 2019b), and TF-VAEGAN (Narayan et al., 2020) on ZSL and GZSL settings. As shown in Table 2, our APN is comparable to or better than SOTA non-generative methods in terms of ZSL accuracy. It indicates that our model learns an image representation that generalizes better to unseen classes. In the more challenging generalized ZSL setting, our APN achieves impressive gains over

state-of-the-art non-generative models for the harmonic mean (H): we achieve 69.4% on CUB and 37.5% on SUN. On AWA2, it obtains 69.6%, which is even better than other generative models, e.g. **LisGAN** with 62.3%, **CLSWGAN** with 59.6%, and **FREE** with 67.1%. This shows that our network is able to balance the performance of seen and unseen classes well, since our attribute prototypes enforce local features to encode visual attributes facilitating more effective knowledge transfer.

Image features extracted from our model also boosts the performance of generative models that synthesize CNN image features for unseen classes. We choose five SOTA methods **ABP** (Zhu et al., 2019b), **GDAN** (Huang et al., 2019), **CVC** (Li et al., 2019b), **f-VAEGAN-D2** (Xian et al., 2019b), and **TF-VAEGAN** (Narayan et al., 2020) as generative models, and follow the same training and evaluation protocol as stated in these approaches. For fair comparison, we train these models with *finetuned features* (Xian et al., 2019b) extracted from ResNet101 (denoted with *). We also report the setting where the feature generating models are trained with our *APN feature* $g(x)$ (e.g. **APN + TF-VAEGAN**).

In the ZSL setting, we observe the following. First, for five generative models, our **APN** consistently boosts their performance on three datasets. For instance, for AWA2, we improve the accuracy of **ABP** from 68.5% to 73.8%, the performance of **CVC** from 64.6% to 71.2%. On the fine-grained datasets CUB and SUN, we also gain performance, e.g. the accuracy of **ABP** is improved from 70.7% to 73.3% on CUB, from 62.6% to 63.1% on SUN. This indicates that compared to standard finetuning with only cross-entropy loss, our *APN features* provide more local information helping the generative models to synthesize discriminative image features. In the GZSL setting, the model predicts both seen and unseen images. We observe that applying our feature to the generative models consistently boosts the harmonic mean, e.g. we improve **ABP** by 2.7% (CUB) and 2.3% (AWA2). Training with our *APN feature* achieves a more balanced accuracy with much better performance on unseen classes. Compared to **CVC*** on AWA2, **APN+CVC** gains 5.8% on unseen while sacrificing only 2.1% on seen. These results demonstrate that our learned locality-enforced image representation lends itself better for knowledge transfer from seen to unseen classes, as the attribute decorrelation loss achieves de-biasing the label prediction.

4.2 Attribute and part localization in ZSL setting

We first evaluate the part localization capability of our method quantitatively. We provide an ablation study

and comparison with other methods in CUB (Wah et al., 2011). In addition, we provide qualitative results of attribute localization on three benchmark datasets. Two user studies are performed to evaluate the accuracy and semantic consistency of attribute similarity maps.

4.2.1 Body part localization

Given the attribute similarity maps related to six body parts of birds, we report the part localization accuracy by calculating the Percentage of Correctly Localized Parts (PCP) following SGMA (Zhu et al., 2019c). As shown in Figure 3, the bounding box marks the image region with the highest attention in each attribute similarity map, then compared with the ground truth part annotation provided by the CUB (Wah et al., 2011) dataset.

Ablation study. We evaluate the effectiveness of our **APN** framework in terms of the influence of the attribute regression loss \mathcal{L}_{Reg} , attribute decorrelation loss \mathcal{L}_{AD} , the similarity compactness loss \mathcal{L}_{CPT} , and the **ZoomInMod**. As shown in Table 1 (right), when trained with the joint losses, **APN** significantly improves the accuracy of *breast*, *head*, *wing* and *leg* by 27.5%, 44.5%, 13.2%, and 32.6% respectively, while the accuracy of *belly* and *back* are improved less. This observation agrees with the qualitative results in Figure 3 that **BaseMod** tends to focus on the center body of the bird, while **APN** results in more accurate and concentrated attention maps. Moreover, \mathcal{L}_{AD} boosts the localization accuracy, which highlights the importance of encouraging in-group similarity and between-group diversity when learning attribute prototypes.

Comparing with SOTA. We report PCP in Table 3. As the baseline, we train a single **BaseMod** with cross-entropy loss \mathcal{L}_{CLS} , and use gradient-based visual explanation method **CAM** (Zhou et al., 2016) to investigate the image area **BaseMod** used to predict each attribute. As state of the art, we report the part localization accuracy of a fine-grained classification model **SPDA-CNN** (Zhang et al., 2016a) which contains a bird part detection branch supervised by parts annotations. In the last two rows, we compare with the weakly supervised model (without part annotation) **SGMA** (Zhu et al., 2019c), which learns part attention for *head* and *leg* by clustering feature channels.

On average, our **APN** improves PCP over **BaseMod** by 22.7% (53.4% vs 30.7%). The majority of the improvements come from better leg and head localization, e.g. from 24.2% to 68.7% (head), and from 16.5% to 49.1% (leg). Compared to the supervised method **SPDA-CNN**, our method achieves comparable accuracy on *breast* and *wing*. Although there is still a gap to the

Method	Parts Annotation	BB size	Breast	Belly	Back	Head	Wing	Leg	Mean
SPDA-CNN (Zhang et al., 2016a)	✓	1/4	67.5	63.2	75.9	90.9	64.8	79.7	73.6
BaseMod (uses \mathcal{L}_{CLS})	✗	1/4	40.3	40.0	27.2	24.2	36.0	16.5	30.7
APN (Ours)			67.8	55.9	29.4	68.7	49.2	49.1	53.4
SGMA (Zhu et al., 2019c)	✗	$1/\sqrt{2}$	—	—	—	74.9	—	48.1	61.5
APN (Ours)			88.1	81.3	71.6	91.4	76.2	70.8	79.9

Table 3: Body part localization in CUB dataset. We comparing our APN with detection model SPDA-CNN trained with part annotations (row 2), and a ZSL model SGMA. The baseline BaseMod takes the original image feature $g(x)$ as input and is trained with \mathcal{L}_{CLS} . For BB (bounding box) size, 1/4 means each part bounding box has the size $\frac{1}{4}W_b \times \frac{1}{4}H_b$, where W_b and H_b are the width and height of the bird. We use gradient-based visual explanation method CAM to visualize the attribute attention map for the baseline BaseMod. For a fair comparison, we use the same evaluation protocol as SGMA in the last two rows.

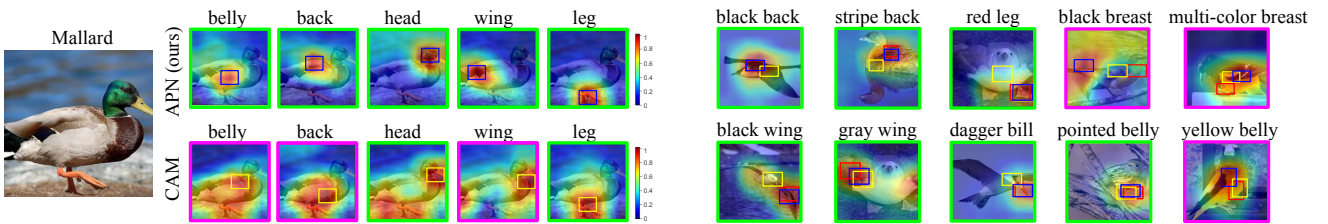


Fig. 3: Part and attribute localization on CUB. Left: Attention maps for each body part of Mallard generated by our APN (first row) and the baseline model BaseMod visualized by CAM (BaseMod(C), second row). Boxes mark out the area with the highest attention. Attention maps are min-max normalized for visualization. Right: Various attribute similarity maps generated by our model. Red, blue, yellow bounding boxes in the image represent the ground truth part bounding box, our results, and the results of BaseMod(C) respectively. Green (purple) box outside the image indicates a correct (incorrect) localization.

supervised method SPDA-CNN, especially on the *back* and *leg* which are hard to localize, the results are encouraging since we do not need require part annotation during training. Since the feature channels encode more pattern information rather than local information (Geirhos et al., 2019; Zhou et al., 2018), enforcing locality over spatial dimension is more accurate than over channel. Under the same evaluation protocol, we significantly improve the localization accuracy over SGMA (79.9% vs 61.5% on average). Besides, our model is able to localize attributes related to six body parts, while SGMA can only localize two main parts.

4.2.2 Qualitative results

Our model localizes attributes by inspecting the attention maps produced by the attribute prototypes. In this section, we qualitatively investigate the part localization ability on the CUB dataset, as well as the attribute localization results on three benchmark datasets.

Part localization in CUB. We first investigate the difference between our APN and the baseline BaseMod for localizing different body parts in CUB dataset. In Figure 3 (left), for each part of the bird Mallard,

we display one attribute similarity map generated by our model APN, and the baseline model BaseMod visualized by CAM (BaseMod(C)). The baseline model tends to generate disperse attention maps covering the whole bird, as it utilizes more global information, e.g. correlated bird parts and context, to predict attributes. For instance, when predicting attributes of *belly* and *back*, the baseline model utilizes pixels scattered on the bird body. On the other hand, the similarity maps of our APN are more concentrated and diverse and therefore they localize different bird body parts more accurately. The improvement is lead by the attribute prototypes and compactness loss, which helps the model to focus on local image features when learning attributes.

Attribute localization in CUB. In addition, unlike other models (Zhang et al., 2016a; Uijlings et al., 2013; Zhu et al., 2019c) that can only localize body parts, our APN model can provide attribute-level localization for CUB dataset, as shown in Figure 3 (right). Our model can localize back with various shapes (row 1, column 1 and 2) and wings with different postures (row 2, column 1 and 2). We can also locate the *pointed belly* of the occluded bird (row 2, column 4). Compared

with **BaseMod(C)**, our approach produces more accurate bounding boxes that localize the predicted attributes. For example, while **BaseMod(C)** wrongly learns the *red leg* from the image region of the belly (row 1, column 3), our model precisely localizes the *red leg* at the correct region. Specifically, when predicting the attributes for wings and legs, the model tends to focus on both two wings and legs even when they are physically separated (row 1, column 3 for *red leg* and row 2, column 2 for *gray wing*). These results are interesting because our model is trained on only class-level attributes without accessing any bounding box annotation.

As a side benefit, the attribute localization ability introduces a certain level of interpretability that supports the zero-shot inference with attribute-level visual evidence. The last two columns in Figure 3 (right) show some failure examples where our model makes wrong predictions. For example, when the yellow breast is wrongly predicted as black (row 1, column 4), the attention map tends to spread over the tail and background; when the black breast is recognized as multi-colored (row 1, column 5), the attention map points to the region of the black and white wing. Besides, although our attribute decorrelation loss in Equation 5 alleviates the correlation issue to some extent (as shown in the previous results in Table 1 and Figure 2), we observe that our **APN** seems to still conflate the *yellow belly* and *yellow breast* (row 2, column 5) in some cases, indicating the attribute correlation issue as a challenging problem for future research.

Attribute localization in AWA2 and SUN. To show how these observations generalize in two other datasets, in Figure 4, we compare our **APN** model with two baseline models on AWA2 and SUN. The attribute attention maps of **BaseMod** is generated with two gradient-based visual explanation method **CAM** (Zhou et al., 2016) and **Grad-CAM** (Selvaraju et al., 2017).

In AWA2 dataset (Figure 4, left), our network produces precise similarity maps for visual attributes that describe *texture* and *body parts*, etc. We can localize visual attributes with diverse appearances, e.g. the white and black *stripe* of zebra, and the yellow and black *stripe* of tiger (row 2, column 3,4), while **CAM** and **Grad-CAM** fails in localizing the stripe on tigers. Our similarity maps for *furry* and *longleg* can precisely mask out the image regions of the ox and horse (row 2, column 3,4), while **BaseMod** only localizes part of the image (row 1, column 3,4). On AWA2 dataset we are interested in the visual attributes of animals, while our model in some cases highlights the attributes of the background, e.g. identifying the grid on the rat cage as stripes (row 2, column 5). This can be explained by the fact that our

	Methods	Results
Accuracy	APN vs CAM	76.0% vs 24.0% ($\pm 5.1\%$)
	APN vs Grad-CAM	74.4% vs 25.6% ($\pm 2.9\%$)
Semantic	CAM	55.0% ($\pm 3.2\%$)
consistency	Grad-CAM	60.0% ($\pm 5.5\%$)
	APN	89.0% ($\pm 3.7\%$)

Table 4: User study results. Top: the percentage of time that one method is marked as more accurate than the other one by users. Bottom: the percentage of attention maps that can be correctly associated with the target attribute by users. **APN**, **CAM**, and **Grad-CAM** denote our model, baseline model visualized by **CAM** (Zhou et al., 2016), and **Grad-CAM** (Selvaraju et al., 2017) respectively.

model only relies on weak supervision, i.e. class-level attributes and their semantic relatedness.

The attribute similarity maps on SUN dataset are shown in figure 4 (right). Our model can discriminate between different attributes with similar color or texture, e.g. correctly locating *snow* and *cloud* in one image (row 2, column 2,3). The baseline models, on the other hand, cannot distinguish between cloud and snow. Although the appearance of one visual attribute may vary significantly, we can still locate them correctly, e.g. the *fencing* with different colors, location, and shape (row 2, column 4,5). Overall, those results indicate that we can perform attribute localization in a weakly supervised manner and provide visual evidence for the inference process of ZSL.

4.2.3 User study

Since the CUB dataset is the only one among the datasets considered here that contains ground truth parts, we design two user studies to assess the accuracy and semantic consistency of attribute attention maps from SUN and AWA2 datasets. We compare the performance of our **APN** model and the baseline **BaseMod** visualized by two model explanation methods, **Grad-CAM** and **CAM**, respectively.

Accuracy of attribute localization. The goal is to evaluate whether the attribute attention maps precisely attend to the related image area. As shown in Figure 5 (left), each test is a tuple $(M_{APN}^i, M_{BaseMod}^i, a_i)$ for attribute a_i , where M_{APN}^i is the attribute attention maps generated by our **APN** model, and $M_{BaseMod}^i$ by the **BaseMod**. The human annotators are presented with the tuple and they are asked to choose the attention map that more accurately covers the attribute region. We randomly sample 50 attention maps from our **APN** model for 20 visual attributes, then generate the corresponding

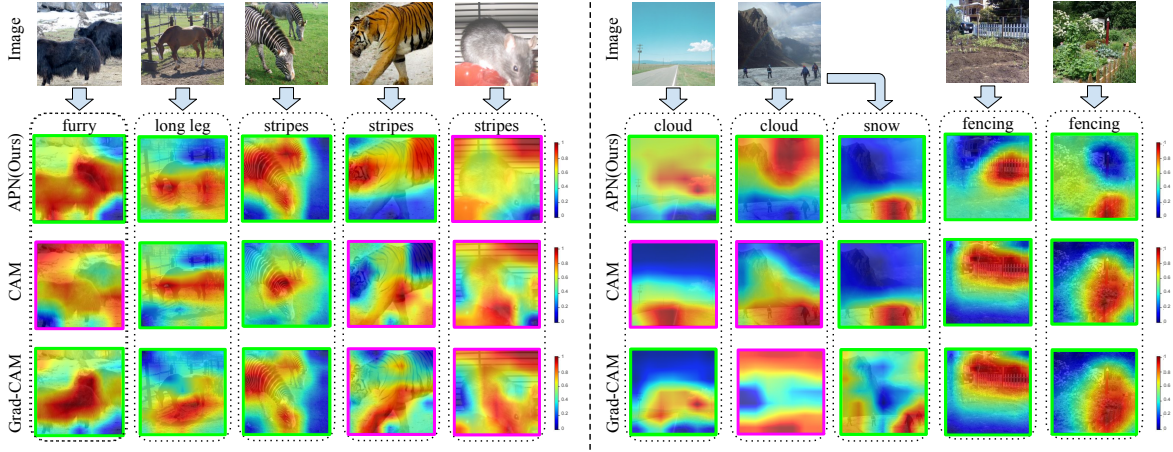


Fig. 4: Attribute attention maps for AWA2 (left) and SUN (right) from our APN model (row 2), BaseMod visualized with CAM (row 3), and BaseMod with Grad-CAM (row 4). The attribute similarity maps are min-max normalized for visualization. We cover the upsampled attention map on the original image, to show the corresponding location of the highlighted area. Green (purple) box outside the image indicates a correct (incorrect) localization.

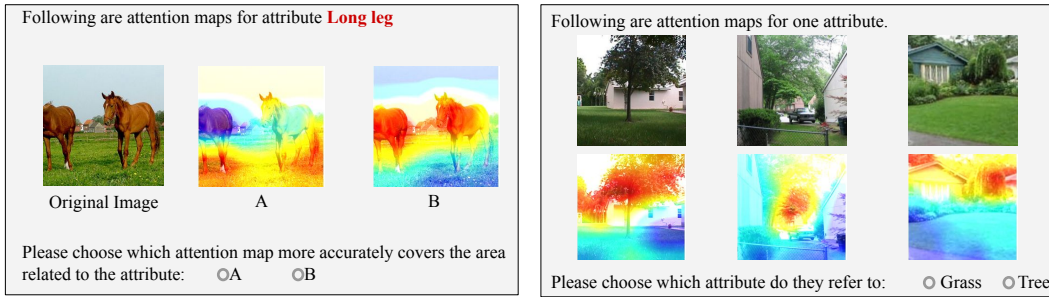


Fig. 5: User Study. Left: User study interface to evaluate the accuracy. Participants are required to choose the attention map that more accurately covers the attribute related region from two attention maps generated by our APN model and the BaseMod (in random position). Right: User study interface for the semantic consistency. Given three attention maps generated for an attribute, the user selects from two candidate attributes which one is the target of the attention maps.

Grad-CAM and CAM attention maps for BaseMod, and create 100 tuples in total. Two separate experiments are performed to compare our APN model with the BaseMod visualized by Grad-CAM and CAM. For each experiment, we employed 5 annotators, i.e. in total 10 students (4 female) aged between 20 and 30 and majoring in computer science participated in the experiment.

We average the responses from each participant and report the standard deviation between each participant as well as the overall accuracy in Table 4 (top). As for the result, our APN attribute attention maps outperform the BaseMod by a large margin. When comparing the attribute attention maps generated by our APN model and the BaseMod visualized by CAM, in 76.0% cases, APN are marked as more accurately covers the attribute-related area than CAM. And in 74.4% cases, APN are more accurate than Grad-CAM. The user study results

agree with the qualitative results in Figure 4 that APN demonstrates more accurate attribute attention maps than the baseline model.

Semantic consistency. Here, our aim is to measure whether the attention maps on different images for one attribute is semantically consistent and can be understood by human. Each test is a tuple $(\mathcal{M}^i, a_i, a_j)$, where a_i is the target attribute, and a_j is a distractor attribute that is semantically similar to a_i . $\mathcal{M}^i = \{M_1^i, M_2^i, M_3^i\}$ is a random subset of attribute attention maps for the target attribute a_i . As shown in Figure 5 (right), the human annotators are presented with the tuple via a user interface, and their task is to identify which of the attributes does the attention map refer to. The performance is defined as the average accuracy of solving such tasks correctly. We sample 20 tuples for three methods (APN, BaseMod+CAM and

BaseMod+Grad-CAM) with two criterion: 1) the evaluated original image and attributes stay the same for the three methods, 2) the target a_0 and distractor a_1 attributes all appear in the original images. Three experiments are performed to evaluate the three methods. There are five annotators for each test, and in total 10 students (4 female) aged between 20 and 30 and majoring in computer science participated in the experiment.

We average the responses from each user and report their overall accuracy and standard deviation between each user in Table 4 (bottom). The user study results indicate high semantic consistency for our model. APN attention maps can be associated with the correct attribute in 89.0% cases, while attention maps from **BaseMod+CAM** only achieve 55.0% accuracy. **BaseMod+Grad-CAM** gains a higher result, at 60.0%, but is still 29.0% lower than ours. The results indicate that our model is able to generate attribute attention maps that are semantic coherent, and can be understood by human. Although the distractor attribute a_0 shares a very similar semantic meaning with the correct attribute (as shown in Figure 5 (right)), APN attention maps can still help users to find the correct answer.

4.3 Few-shot learning

In the few-shot learning (FSL) scenario, the images are divided into base classes where plenty of training samples can be obtained and novel classes with only a handful of training samples. The goal of FSL is to learn a classifier to recognize novel classes with limited labeled examples. In the generalized few-shot learning (GFSL) setting, the classifier is trained to recognize images from both base and novel classes.

Compared methods. In this section, we evaluate our attribute prototype network under two evaluation protocols, i.e. the all-way evaluation and N-way-K-shot evaluation. In the all-way evaluation, our model is compared with several state-of-the-art generative FSL methods. **Analogy** (Hariharan and Girshick, 2017), **f-VAEGAN-D2** (Xian et al., 2019b) and **TF-VAEGAN** (Narayan et al., 2020) are data synthesis based methods that augment image features for novel classes. **Imprinted** (Qi et al., 2018) directly uses the normalized activation of novel images as the classifier weight. For a fair comparison, these models are trained with *finetuned feature* extracted from ResNet101, and under the same dataset split (Xian et al., 2019b). In the FSL setting, we report the averaged top-1 accuracy for novel classes with the model that only predicts novel classes. In the GFSL setting, we report the averaged

top-1 accuracy of test samples of all classes, where the model predicts both base and novel classes labels.

In the N-way-K-shot evaluation, we build our attribute prototype network over the ResNet12 (He et al., 2016) backbone in DPGN (Yang et al., 2020), and train the network with both the FSL training losses (Yang et al., 2020) and our \mathcal{L}_{APN} loss. Our model is compared with state-of-the-art FSL methods under the N-way-K-shot evaluation. **MatchingNet** (Vinyals et al., 2016), **ProtoNet** (Snell et al., 2017) and **CloserLook** (Fu et al., 2017) propose to optimize the representation learning model with metric learning methods. **MAML** (Finn et al., 2017) learns to initialize the model weight so that it can adapt to novel classes efficiently. Two latest methods further enhance the meta-learning approach with graph network (Yang et al., 2020) and attention agent trained with reinforcement learning (Hong et al., 2021). We report the top-1 accuracy in the 5way-1shot and 5way-5shot setting following (Yang et al., 2020).

Comparing with the SOTA. We display the few-shot learning accuracy in Table 5. Under the all-way evaluation setting, our model yields consistent improvement on three datasets, i.e. CUB, AWA2, and SUN. On AWA2 dataset, compared to **TF-VAEGAN** trained with *finetuned feature*, our model **APN+TF-VAEGAN** improve the FSL accuracy of by a large margin, especially in the low-shot scenario where only a small number of samples from novel classes are available, i.e. we gain 9.9% (1-shot), 8.4% (2-shot), 7.0% (5-shot), and 6.2% (10-shot). On fine-grained dataset CUB, our *APN feature* yields consistent improvement over the *finetuned feature*. Compared to **f-VAEGAN-D2** trained with *finetuned feature*, our model **APN+f-VAEGAN-D2** gain 1.7% (1-shot), 1.5% (2-shot), 1.4% (5-shot), and 1.2% (10-shot) on FSL. The same trend is observed on SUN dataset. Though the accuracy for the 1-shot and 2-shot regime are comparable to other methods, we manage to improve a lot when training samples increase, e.g. our model **APN+TF-VAEGAN** achieves 74.1% (5-shot) and 76.0% (10-shot), compared to **TF-VAEGAN** with 68.9% (5-shot) and 74.0% (10-shot).

Compared to other FSL models, we gain significant improvements. For instance, we achieve 77.8% (1-shot) on FSL for CUB dataset, compared to 48.5% (**Analogy**) and 56.5% (**Imprinted**). For AWA2 dataset, we gain 87.2% on FSL, compared to 66.9% (**Analogy**) and 62.5% (**Imprinted**). Specifically, our model using one labeled image per class approaches the accuracy of **Analogy** and **Imprinted** trained with five samples. It indicates that improving the locality of image features can better help the feature generators to mimic the real data distribution. When increasing the number of training samples (i.e. in the 10-shot scenario), the

Method	AWA2				CUB				SUN			
	1	2	5	10	1	2	5	10	1	2	5	10
Analogy (Hariharan and Girshick, 2017)	62.5	81.3	82.4	87.8	56.5	69.5	78.0	81.1	40.0	49.0	67.6	75.5
Imprinted (Qi et al., 2018)	66.9	82.6	89.0	93.5	48.5	65.0	80.0	85.3	37.9	47.8	62.1	70.2
f-VAEGAN-D2 (Xian et al., 2019b)	75.0	87.9	90.5	93.1	76.1	79.6	83.4	85.9	68.8	69.5	70.0	70.9
APN+f-VAEGAN-D2 (Ours)	82.1	92.4	94.2	95.6	77.8	81.1	84.8	87.1	68.2	69.4	72.4	75.1
TF-VAEGAN (Narayan et al., 2020)	77.3	84.4	87.7	89.8	75.6	81.1	83.5	85.6	68.1	68.5	68.9	74.0
APN+TF-VAEGAN (Ours)	87.2	92.8	94.7	96.0	77.1	82.6	85.2	86.6	68.8	69.9	74.1	76.0

Table 5: Few-shot learning results. We apply our *APN features* to feature generation model (i.e. APN+f-VAEGAN-D2 and APN+TF-VAEGAN) and compare with other data synthesis based models. Note that f-VAEGAN-D2 (Xian et al., 2019b) and TF-VAEGAN (Narayan et al., 2020) generate image features given the class attributes to augment the training of novel classes. Our APN model uses the same attributes to learn locality enhanced image features.

Method	AWA2				CUB				SUN			
	1	2	5	10	1	2	5	10	1	2	5	10
Analogy (Hariharan and Girshick, 2017)	55.0	64.7	70.7	74.5	54.1	67.5	75.5	79.5	37.5	39.6	42.4	44.6
Imprinted (Qi et al., 2018)	44.7	50.5	70.0	88.1	57.0	67.5	75.5	79.5	37.7	38.9	42.4	42.5
f-VAEGAN-D2 (Xian et al., 2019b)	72.7	80.7	85.6	88.9	71.1	74.5	77.6	79.7	43.5	43.5	43.2	44.9
APN+f-VAEGAN-D2 (Ours)	74.6	83.3	86.9	89.7	72.1	76.1	79.3	80.9	43.1	44.0	45.5	45.9
TF-VAEGAN (Narayan et al., 2020)	74.7	81.1	86.0	87.1	70.6	74.7	77.5	79.3	43.3	42.3	42.9	45.4
APN+TF-VAEGAN (Ours)	80.1	85.9	88.6	90.3	71.7	76.4	78.9	80.4	44.3	42.9	46.1	46.7

Table 6: Generalized few-shot learning results. We apply our *APN features* to feature generation model (i.e. APN+f-VAEGAN-D2 and APN+TF-VAEGAN) and compare with other data synthesis based models.

distance between the other three methods shrinks as we are going towards the fully supervised setting. However, our model still manages to improve the performance, which denotes that even with abundant training samples, locality enhanced image features will train a more discriminative classifier than ordinary features.

The locality augmented model generates discriminative features for novel classes, especially when applied to the generalized setting where the model should predict both base and novel classes. As shown in Table 6, on AWA2 dataset, our model APN+TF-VAEGAN gains accuracy improvement for 5.4% (1-shot), 4.8% (2-shot), 2.6% (5-shot), and 3.2% (10-shot). The results demonstrate that our model generates highly discriminative image features by leveraging attribute information. In CUB dataset, we gain 1.0% (1-shot), 1.6% (2-shot), 1.7% (5-shot), and 1.1% (10-shot). In SUN dataset, we also manage to improve the accuracy consistently, e.g. we gain 1.0% (1-shot), 0.7% (2-shot) and 3.2% (5-shot), and 1.3% (10-shot) on GFSL.

As shown in Table 7, in the N-way-K-shot scenario where we train DPGN (Yang et al., 2020) with our attribute prototype network, we yield improvement over the baseline DPGN on CUB and achieve new state-of-the-art accuracy. We achieve 77.4% (5way-1shot), compared to 68.4% (CloserLook), 74.1% (RAP+ProtoNet) and 75.7% (DPGN). In the 5way-5shot setting, we also

Method	Backbone	5way-1shot	5way-5shot
MatchingNet*	ResNet18	72.4 ± 0.90	83.6 ± 0.60
ProtoNet*	ResNet18	73.0 ± 0.88	86.6 ± 0.51
MAML*	ResNet18	68.4 ± 1.07	83.5 ± 0.62
CloserLook	ConvNet	60.5 ± 0.83	79.3 ± 0.61
ArL	ConvNet	50.6	65.9
RAP+ProtoNet	ResNet18	74.1 ± 0.60	89.2 ± 0.31
RAP+Neg-Margin	ResNet18	75.4 ± 0.81	90.6 ± 0.39
DPGN	ResNet12	75.7 ± 0.47	91.5 ± 0.33
APN+DPGN (Ours)	ResNet12	77.4 ± 0.44	92.2 ± 0.24

Table 7: Few-shot learning results on CUB dataset (* results are from Hong et al. (2021)). Following Yang et al. (2020), we report top-1 accuracy in 5way-1shot/-5shot settings and compare ours with MatchingNet (Vinyals et al., 2016), ProtoNet (Snell et al., 2017), MAML (Finn et al., 2017), CloserLook (Fu et al., 2017), ArL (Zhang et al., 2021b), RAP+ProtoNet (Hong et al., 2021), RAP+Neg-Margin (Hong et al., 2021), DPGN (Yang et al., 2020).

improve over CloserLook, RAP+ProtoNet and DPGN by 12.9%, 3.0% and 0.7% respectively. The results indicate that integrating attribute prototype network into the representation learning process helps the network to learn locality enhanced features and benefit the FSL performance.

Method	Zero-Shot Learning (ZSL)			Generalized Zero-Shot Learning (GZSL)								
	AWA2	CUB	SUN	AWA2			CUB			SUN		
	T1	T1	T1	u	s	H	u	s	H	u	s	H
CADA-VAE (Schonfeld et al., 2019b)	49.0	22.5	37.8	38.6	60.1	47.0	16.3	39.7	23.1	26.0	28.2	27.0
SJE (Akata et al., 2015b)	53.7	14.4	26.3	39.7	65.3	48.8	13.2	28.6	18.0	19.8	18.6	19.2
GEM-ZSL (Liu et al., 2021)	50.2	25.7	—	40.1	80.0	53.4	11.2	48.8	18.2	—	—	—
APN(w2v) (Ours)	59.6	27.7	32.1	41.8	75.0	53.7	20.6	26.4	23.4	20.3	21.3	20.8

Table 8: Zero-Shot Learning results from our APN model and other state-of-the-art on CUB, AWA2, and SUN datasets. All the models are trained with unsupervised class embedding, i.e. w2v. SJE (Akata et al., 2015b), GEM-ZSL (Liu et al., 2021), and our model APN are non-generative models, while CADA-VAE (Schonfeld et al., 2019b) is feature generation model. We measure top-1 accuracy (T1) in ZSL, top-1 accuracy on seen/unseen (s/u) classes and their harmonic mean (H) in GZSL.

Method	Few-Shot Learning					Generalized Few-Shot Learning				
	1	2	5	10	20	1	2	5	10	20
softmax	49.3	64.5	76.7	81.0	84.2	50.0	60.8	73.5	79.0	80.7
Analogy (Hariharan and Girshick, 2017)	40.5	50.7	61.6	69.5	76.0	51.5	59.8	67.4	72.0	77.3
f-VAEGAN-D2-ind (Xian et al., 2019b)	54.4	64.4	74.6	79.9	84.0	60.3	65.7	73.5	78.8	79.5
f-VAEGAN-D2 (Xian et al., 2019b)	60.1	70.0	79.0	81.5	84.5	66.3	72.6	78.6	81.5	83.2
APN(w2v)+f-VAEGAN-D2	61.7	70.9	79.5	83.4	85.5	67.5	73.8	79.6	82.5	84.3

Table 9: Few-Shot Learning results on ImageNet with increasing number of training samples per novel class (top-5 accuracy). Our APN(w2v) model is trained with w2v class embeddings. We apply our APN features to feature generation model (i.e. APN(w2v)+ f-VAEGAN-D2).

4.4 Discussion

We study the flexibility of our APN network by using only unsupervised embeddings, e.g. word2vec (w2v) (Mikolov et al., 2013). Similar to learning attributes, for w2v with 300 dim, we design 300 prototypes in the ProtoMod. Since there is no grouping for w2v, we discard the attribute decorrelation loss \mathcal{L}_{AD} when training the model.

We compare the zero-shot learning results of our APN model with other state-of-the-art models in Table 8. The performance of using w2v as the class embeddings could drop compared to attributes. But this issue exists in most zero-shot learning methods, as shown in Table 8. In general, our method can be generalized to unsupervised class embeddings and still outperforms the baselines using w2v. For instance, we outperform other non-generative models such as SJE and GEM-ZSL on three datasets, e.g. we achieve 59.6% on AWA2, comparing with SJE with 53.7% and GEM-ZSL with 50.2%. Our model even outperform generative model CADA-VAE that synthesize image features on AWA2 and CUB dataset.

We perform few-shot learning on ImageNet to study the generalization ability of our model on the large-scale dataset. We follow the data split in Xian et al. (2019b) where the 1K ImageNet categories are randomly divided into 389 base classes and 611 novel classes. We use the

300-dim word2vec (Mikolov et al., 2013) embeddings as the class embedding for ImageNet since there is no attribute annotation. Our APN model is trained with train samples from the base classes. The results shown in Table 9 demonstrate that our APN model trained with only w2v learns better representations and further boosts the few-shot learning performance on the large-scale ImageNet dataset. Notably, we gain 1.6% (1-shot) on FSL and 1.2% (1-shot) on GFSL.

5 Conclusion

In this work, we develop a representation learning framework for zero-shot learning and few-shot learning, i.e. attribute prototype network (APN), to jointly learn global and local features. Our model improves the locality of image representations by regressing attributes with local features and decorrelating prototypes with regularisation. We explicitly encourage the network to learn from informative attribute related image regions and discard noisy backgrounds by cropping the original image with attribute similarity maps. We demonstrate consistent improvement over the state-of-the-art on three benchmarks. And our representations improve over finetuned ResNet representations when used in conjunction with feature generating models. We qualitatively verify that our network is able to localize

attributes in images accurately. Two well-designed user studies indicate that our network can generate semantically consistent and accurate attribute attention maps. The part localization accuracy significantly outperforms a weakly supervised localization model designed for zero-shot learning. We further show that our model can be extended to the FSL scenario, and we consistently improve the classification accuracy in any-shot regimes on three datasets.

Acknowledgements This work has been partially funded by the ERC 853489 - DEXIM and by the DFG – EXC number 2064/1 – Project number 390727645.

References

- Akata Z, Perronnin F, Harchaoui Z, Schmid C (2015a) Label-embedding for image classification. *IEEE TPAMI* 38(7)
- Akata Z, Reed S, Walter D, Lee H, Schiele B (2015b) Evaluation of output embeddings for fine-grained image classification. In: *CVPR*
- Anderson P, He X, Buehler C, Teney D, Johnson M, Gould S, Zhang L (2018) Bottom-up and top-down attention for image captioning and visual question answering. In: *CVPR*
- Arik SO, Pfister T (2019) Attention-based prototypical learning towards interpretable, confident and robust deep neural networks. *arXiv:190206292*
- Cacheux YL, Borgne HL, Crucianu M (2019) Modeling inter and intra-class relations in the triplet loss for zero-shot learning. In: *ICCV*
- Changpinyo S, Chao WL, Gong B, Sha F (2016) Synthesized classifiers for zero-shot learning. In: *CVPR*
- Changpinyo S, Chao WL, Gong B, Sha F (2020) Classifier and exemplar synthesis for zero-shot learning. In: *IJCV*
- Chao WL, Changpinyo S, Gong B, Sha F (2016) An empirical study and analysis of generalized zero-shot learning for object recognition in the wild. In: *ECCV*
- Chen C, Li O, Tao D, Barnett A, Rudin C, Su JK (2019a) This looks like that: deep learning for interpretable image recognition. In: *NeurIPS*
- Chen S, Wang W, Xia B, Peng Q, You X, Zheng F, Shao L (2021) Free: Feature refinement for generalized zero-shot learning. In: *ICCV*
- Chen WY, Liu YC, Kira Z, Wang YCF, Huang JB (2019b) A closer look at few-shot classification. *ICLR*
- Deng J, Dong W, Socher R, Li LJ, Li K, Fei-Fei L (2009) Imagenet: A large-scale hierarchical image database. In: *CVPR*
- Finn C, Abbeel P, Levine S (2017) Model-agnostic meta-learning for fast adaptation of deep networks. *ICML*
- Finn C, Xu K, Levine S (2018) Probabilistic model-agnostic meta-learning. In: *NeurIPS*
- Fu J, Zheng H, Mei T (2017) Look closer to see better: Recurrent attention convolutional neural network for fine-grained image recognition. In: *CVPR*
- Gao T, Han X, Liu Z, Sun M (2019) Hybrid attention-based prototypical networks for noisy few-shot relation classification. In: *AAAI*
- Geirhos R, Rubisch P, Michaelis C, Bethge M, Wichmann FA, Brendel W (2019) Imagenet-trained cnns are biased towards texture; increasing shape bias improves accuracy and robustness. *ICLR*
- Guan J, Lu Z, Xiang T, Li A, Zhao A, Wen JR (2020) Zero and few shot learning with semantic feature synthesis and competitive learning. *IEEE TPAMI*
- Guo Y, Ding G, Han J, Tang S (2018) Zero-shot learning with attribute selection. In: *AAAI*
- Hariharan B, Girshick R (2017) Low-shot visual recognition by shrinking and hallucinating features. In: *IEEE ICCV*
- He K, Zhang X, Ren S, Sun J (2016) Deep residual learning for image recognition. In: *CVPR*
- Hjelm RD, Fedorov A, Lavoie-Marchildon S, Grewal K, Bachman P, Trischler A, Bengio Y (2019) Learning deep representations by mutual information estimation and maximization. *ICLR*
- Hong J, Fang P, Li W, Zhang T, Simon C, Harandi M, Petersson L (2021) Reinforced attention for few-shot learning and beyond. In: *CVPR*
- Huang H, Wang C, Yu PS, Wang CD (2019) Generative dual adversarial network for generalized zero-shot learning. In: *IEEE CVPR*
- Jayaraman D, Sha F, Grauman K (2014) Decorrelating semantic visual attributes by resisting the urge to share. In: *CVPR*
- Jiang H, Wang R, Shan S, Chen X (2019) Transferable contrastive network for generalized zero-shot learning. In: *ICCV*
- Kim JH, Jun J, Zhang BT (2018) Bilinear attention networks. In: *NeurIPS*
- Kingma DP, Ba J (2015) Adam: A method for stochastic optimization. *ICLR*
- Kumar Verma V, Arora G, Mishra A, Rai P (2018) Generalized zero-shot learning via synthesized examples. In: *CVPR*
- Lampert CH, Nickisch H, Harmeling S (2009) Learning to detect unseen object classes by between-class attribute transfer. In: *CVPR*
- Li A, Lu Z, Guan J, Xiang T, Wang L, Wen JR (2020) Transferrable feature and projection learning with class hierarchy for zero-shot learning. In: *IJCV*

- Li J, Jing M, Lu K, Ding Z, Zhu L, Huang Z (2019a) Leveraging the invariant side of generative zero-shot learning. In: CVPR
- Li K, Min MR, Fu Y (2019b) Rethinking zero-shot learning: A conditional visual classification perspective. In: IEEE ICCV
- Li L, Tang S, Deng L, Zhang Y, Tian Q (2017) Image caption with global-local attention. In: AAAI
- Li O, Liu H, Chen C, Rudin C (2018a) Deep learning for case-based reasoning through prototypes: A neural network that explains its predictions. In: AAAI
- Li Y, Zhang J, Zhang J, Huang K (2018b) Discriminative learning of latent features for zero-shot recognition. In: CVPR
- Liu L, Willem A, Chen S, Lovell BC (2014) Automatic image attribute selection for zero-shot learning of object categories. In: ICPR
- Liu S, Long M, Wang J, Jordan MI (2018) Generalized zero-shot learning with deep calibration network. In: NeurIPS
- Liu Y, Guo J, Cai D, He X (2019) Attribute attention for semantic disambiguation in zero-shot learning. In: ICCV
- Liu Y, Zhou L, Bai X, Huang Y, Gu L, Zhou J, Harada T (2021) Goal-oriented gaze estimation for zero-shot learning. In: Proceedings of the IEEE/CVF Conference on Computer Vision and Pattern Recognition, pp 3794–3803
- Mikolov T, Sutskever I, Chen K, Corrado GS, Dean J (2013) Distributed representations of words and phrases and their compositionality. In: NeurIPS
- Munkhdalai T, Yu H (2017) Meta networks. JMLR 70
- Narayan S, Gupta A, Khan FS, Snoek CG, Shao L (2020) Latent embedding feedback and discriminative features for zero-shot classification. ECCV
- Noroozi M, Favaro P (2016) Unsupervised learning of visual representations by solving jigsaw puzzles. In: ECCV
- Oreshkin B, López PR, Lacoste A (2018) Tadam: Task dependent adaptive metric for improved few-shot learning. In: NeurIPS
- Patterson G, Xu C, Su H, Hays J (2014) The sun attribute database: Beyond categories for deeper scene understanding. IJCV
- Qi H, Brown M, Lowe DG (2018) Low-shot learning with imprinted weights. In: CVPR
- Ravi S, Larochelle H (2017) Optimization as a model for few-shot learning. ICLR
- Romera-Paredes B, OX E, Torr PH (2015) An embarrassingly simple approach to zero-shot learning. In: ICML
- Rusu AA, Rao D, Sygnowski J, Vinyals O, Pascanu R, Osindero S, Hadsell R (2019) Meta-learning with latent embedding optimization. ICLR
- Schonfeld E, Ebrahimi S, Sinha S, Darrell T, Akata Z (2019a) Generalized zero-and few-shot learning via aligned variational autoencoders. In: CVPR
- Schonfeld E, Ebrahimi S, Sinha S, Darrell T, Akata Z (2019b) Generalized zero-and few-shot learning via aligned variational autoencoders. In: CVPR
- Selvaraju RR, Cogswell M, Das A, Vedantam R, Parikh D, Batra D (2017) Grad-cam: Visual explanations from deep networks via gradient-based localization. In: ICCV
- Shu Y, Shi Y, Wang Y, Huang T, Tian Y (2020) p-odn: prototype-based open deep network for open set recognition. Scientific Reports 10(1)
- Snell J, Swersky K, Zemel R (2017) Prototypical networks for few-shot learning. In: Neurips
- Sun Y, Zheng L, Yang Y, Tian Q, Wang S (2018) Beyond part models: Person retrieval with refined part pooling (and a strong convolutional baseline). In: ECCV
- Sylvain T, Petrini L, Hjelm D (2020) Locality and compositionality in zero-shot learning. ICLR
- Tang L, Wertheimer D, Hariharan B (2020) Revisiting pose-normalization for fine-grained few-shot recognition. In: IEEE CVPR
- Tokmakov P, Wang YX, Hebert M (2019) Learning compositional representations for few-shot recognition. In: IEEE ICCV
- Uijlings JR, Van De Sande KE, Gevers T, Smeulders AW (2013) Selective search for object recognition. IJCV 104(2)
- Vinyals O, Blundell C, Lillicrap T, Kavukcuoglu K, Wierstra D (2016) Matching networks for one shot learning. In: NeurIPS
- Wah C, Branson S, Welinder P, Perona P, Belongie S (2011) The Caltech-UCSD Birds-200-2011 Dataset. Tech. Rep. CNS-TR-2011-001, California Institute of Technology
- Wan Z, Chen D, Liao J (2021) Visual structure constraint for transductive zero-shot learning in the wild. In: IJCV
- Wang G, Yuan Y, Chen X, Li J, Zhou X (2018a) Learning discriminative features with multiple granularities for person re-identification. In: ACMML
- Wang K, Liew JH, Zou Y, Zhou D, Feng J (2019) Panet: Few-shot image semantic segmentation with prototype alignment. In: ICCV
- Wang Q, Chen K (2017) Zero-shot visual recognition via bidirectional latent embedding. In: IJCV
- Wang YX, Girshick R, Hebert M, Hariharan B (2018b) Low-shot learning from imaginary data. In: CVPR
- Wei C, Xie L, Ren X, Xia Y, Su C, Liu J, Tian Q, Yuille AL (2019) Iterative reorganization with weak spatial constraints: Solving arbitrary jigsaw puzzles

- for unsupervised representation learning. In: CVPR
- Wei XS, Luo JH, Wu J, Zhou ZH (2017) Selective convolutional descriptor aggregation for fine-grained image retrieval. *IEEE TIP* 26(6)
- Xian Y, Akata Z, Sharma G, Nguyen Q, Hein M, Schiele B (2016) Latent embeddings for zero-shot classification. In: CVPR
- Xian Y, Lorenz T, Schiele B, Akata Z (2018) Feature generating networks for zero-shot learning. In: CVPR
- Xian Y, Lampert CH, Schiele B, Akata Z (2019a) Zero-shot learning-a comprehensive evaluation of the good, the bad and the ugly. *TPAMI*
- Xian Y, Sharma S, Schiele B, Akata Z (2019b) f-vaegan-d2: A feature generating framework for any-shot learning. In: CVPR
- Xie GS, Liu L, Jin X, Zhu F, Zhang Z, Qin J, Yao Y, Shao L (2019) Attentive region embedding network for zero-shot learning. In: CVPR
- Xu W, Xian Y, Wang J, Schiele B, Akata Z (2020) Attribute prototype network for zero-shot learning. *NeurIPS*
- Yang HM, Zhang XY, Yin F, Liu CL (2018) Robust classification with convolutional prototype learning. In: CVPR
- Yang L, Li L, Zhang Z, Zhou X, Zhou E, Liu Y (2020) Dpgn: Distribution propagation graph network for few-shot learning. In: CVPR
- Yeh CK, Kim J, Yen IEH, Ravikumar PK (2018) Representer point selection for explaining deep neural networks. In: *NeurIPS*
- Yu Y, Ji Z, Fu Y, Guo J, Pang Y, Zhang ZM, et al. (2018) Stacked semantics-guided attention model for fine-grained zero-shot learning. In: *NeurIPS*
- Zhang F, Li M, Zhai G, Liu Y (2021a) Multi-branch and multi-scale attention learning for fine-grained visual categorization. In: *ICMM*
- Zhang H, Xu T, Elhoseiny M, Huang X, Zhang S, Elgammal A, Metaxas D (2016a) Spda-cnn: Unifying semantic part detection and abstraction for fine-grained recognition. In: CVPR
- Zhang H, Koniusz P, Jian S, Li H, Torr PH (2021b) Rethinking class relations: Absolute-relative supervised and unsupervised few-shot learning. In: CVPR
- Zhang L, Xiang T, Gong S (2017) Learning a deep embedding model for zero-shot learning. In: CVPR
- Zhang X, Xiong H, Zhou W, Lin W, Tian Q (2016b) Picking deep filter responses for fine-grained image recognition. In: CVPR
- Zheng H, Fu J, Mei T, Luo J (2017) Learning multi-attention convolutional neural network for fine-grained image recognition. In: *ICCV*
- Zhou B, Khosla A, Lapedriza A, Oliva A, Torralba A (2016) Learning deep features for discriminative localization. In: CVPR
- Zhou B, Bau D, Oliva A, Torralba A (2018) Interpreting deep visual representations via network dissection. *TPAMI* 41(9)
- Zhu P, Wang H, Saligrama V (2019a) Learning classifiers for target domain with limited or no labels. In: *ICML*
- Zhu Y, Elhoseiny M, Liu B, Peng X, Elgammal A (2018) A generative adversarial approach for zero-shot learning from noisy texts. In: CVPR
- Zhu Y, Xie J, Liu B, Elgammal A (2019b) Learning feature-to-feature translator by alternating back-propagation for generative zero-shot learning. In: *ICCV*
- Zhu Y, Xie J, Tang Z, Peng X, Elgammal A (2019c) Semantic-guided multi-attention localization for zero-shot learning. In: *NeurIPS*